Energy 313 (2024) 133853

Contents lists available at ScienceDirect

Energy

journal homepage: www.elsevier.com/locate/energy

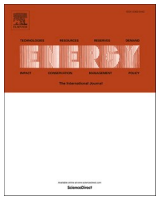

Feasible application of thermoelectric generators in light aviation

Iho López Tobi [a,*], Martí Comamala [a], Lino Montoro [a], Josep Ramon González [a], Jacek Czarnigowski [b], Arantzazu Gómez [c]

[a] University of Girona, Department of Mechanical Engineering and Industrial Construction, Carrer Universitat de Girona, 4, 17003, Girona, Spain
[b] Lublin University of Technology, Department of Thermodynamics, Fluid Mechanics and Aviation Propulsion, Nadbystrzycka 36, 20-618, Lublin, Poland
[c] Castilla-La Mancha University, Toledo School of Industrial and Aerospace Engineering, Royal Weapons Factory, Edif. Sabatini, Av. Carlos III, s/n, Toledo, 45071, Spain

ARTICLE INFO

Handling Editor: Dr. Q. F. Ofelia Araujo

Keywords:
Light aviation
Thermoelectric generators
Engine simulation

ABSTRACT

Energy consumption in aviation is steadily increasing, requiring new technological solutions to reduce emissions and enhance sustainability. To address energy and emission challenges, researchers are exploring thermoelectric devices for thermal energy recovery and direct conversion into electricity. In this study a comprehensive model of the Rotax 912 ULS engine (R912) is implemented using GT-suite software. Through the simulations we estimate exhaust gas temperatures to be used for electrical production using a thermoelectric generator (TEG). The methodology used comprises a set of one dimensional simulations, validated with manufacturer and experimental data. The simulations served to analyze the performance of the engine after coupling the TEG to the exhaust system, and to estimate the electrical power production, under several working conditions. The findings aim to evaluate the feasibility of replacing the engine's alternator with a TEG, potentially reducing aircraft weight, and increasing flight autonomy and range in the field of light aviation.

1. Introduction

Aviation is one of the fastest growing industries [1]. The energy consumption of aerial transport increases by about 5 % per year and it is expected to reach more than 23 EJ in 2040 [2]. This growth is not limited to airliners, it also includes civil and military light aviation subsectors such as ultralight aircraft, small-size planes (4–6 pax) and unmanned aerial vehicles. Their versatility is what makes them stand out to users when choosing their application into specific mission profiles: wildlife surveillance, search and rescue operations or even medical delivery in hard to access areas [3–8]. In Europe, over forty thousand ultralight aircraft have already been manufactured to date in the last 25 years. This emphasizes the importance of contributing towards energy and emission reduction techniques [9,10]. The Strategic Research and Innovation Agenda (SRIA) developed by ACARE, provides a strategic roadmap for aviation research and innovation. The program prioritizes goals related to energy savings, focusing on the development of reliable and low-noise on-board systems for electrical production, either from the main engine or through auxiliary units, without costs and weight penalization [11].

Thermoelectric devices could be an interesting and advantageous option for converting thermal energy into electricity. TEGs offer benefits like low noise, reduced maintenance costs, and weight reduction when compared to alternative energy harvesters [12–15]. In the process of converting heat to electricity, many energy conversion technologies involve intermediate steps. For instance, heat energy from fuel is typically converted first to mechanical energy in a turbine, and subsequently, this mechanical energy is then converted to electricity in a generator. Each of these energy conversion step introduces waste heat losses. This issue is mitigated in TEGs. In the case of unmanned aerial vehicles (UAVs) with a significant electronic payload, the norm is to use propulsion engines as a source of electricity through internal or external alternators. This often leads to an increase in fuel consumption, reducing its flight autonomy [16,17]. TEGs offer a more scalable solution. Such can be designed to produce a wide range of power outputs, from microwatts to kilowatts. In the context of the aviation industry, the demand for energy-efficient solutions is becoming more prominent. The introduction of thermoelectric generators (TEGs) emerges as a promising avenue for addressing energy challenges. Not only aiming to generate scalable electrical power with reduced weight, but also the potential replacement of traditional engine components such as alternators. Existent investigations [18–21] highlight the versatile potential of TEGs across diverse applications within aviation, especially in high-temperature environments found in hypersonic vehicles or jet airliners. The proposed innovative approach, exemplified by a

* Corresponding author.
E-mail address: u1984735@campus.udg.edu (I. López Tobi).

https://doi.org/10.1016/j.energy.2024.133853
Received 5 December 2023; Received in revised form 30 October 2024; Accepted 14 November 2024
Available online 15 November 2024

Abbreviations

1-D	One dimensional
2-D	Two dimensional
ACARE	Advisory Council for Aviation Research and Innovation in Europe
AFR	Air to fuel ratio (kg/kg)
BM	Burned mass (%)
BSFC	Break specific fuel consumption (g/kWh)
CE	Combustion efficiency (%)
DO	Design optimizer
FMEP	Friction mean effective pressure (bar)
ICE	Internal combustion engine
LSU	Lambda sensor unit
LTO	Landing and take off
RPM	revolutions per minute (rev/min)
R912	Rotax 912 ULS engine
SOC	Start of combustion (°)
SRIA	Strategic Research and Innovation Agenda
TDC	Top dead center
TEG	Thermoelectric generator
TEM	Thermoelectric module
UAV	Unmanned aircraft vehicle
ULM	Ultralight manned aircraft
WC	Wiebe constant

multi-stage thermoelectric generator scheme for hypersonic vehicles, emphasizes the adaptability of TEGs to unique aviation settings, particularly when utilizing high-temperature fuel as a heat source. For this study the focus lies in light aviation. This sector often employs internal combustion engine (ICE) manufactured by Rotax, with the R912 being the most common unit in use [22].

An exhaustive simulation model must be built to use modeling techniques that allow engine performance prediction. Simulation software like GT-SUITE has proven useful when utilized to study aircraft engine performance under various conditions. Utilizing data from the engine operation manual, 1-D models have been implemented to generate fuel consumption maps or simulate combustion parameters [23–25]. When coupling a TEG to the R912, it has been demonstrated that it can successfully provide substantial electrical power [26], it is described the use of a one-dimensional model to record engine performance. An approach that has proven the most fitted when conducting these types of engine simulations. Indicating the ability to produce accurate results using 1-D modeling tools [23,24]. Our research aims to contribute novelty to the sector by thoroughly exploring TEG applications within the broader aviation landscape. We focus on demonstrating the versatility and scalability of TEG applications expressly excluding traditional airliners and hypersonic vehicles and focusing on the feasibility of their application and benefits in smaller aircraft. Showcasing how TEGs can effectively transition from high-temperature environments to smaller aviation settings, achieving successful outcomes. Providing practical insights into the adaptability of TEGs within the industry. While our research intentionally avoids the realms of airliners and hypersonic vehicles due to their distinct characteristics and requirements, we recognize the significance of understanding TEGs' versatile application within the broader aviation spectrum. This deliberate distinction clarifies our research scope and positions our study as a valuable addition to the growing body of knowledge regarding the practical implementation of TEGs in aviation contexts, extending beyond the scope of conventional commercial aircraft.

The present study focuses on analyzing the performance parameters of the R912 across a range of continuous engine speeds, including the manufacturer's specified performance range from sea level to 5500 m. The primary objective of this research is to assess the potential benefits derived from attaching an automobile thermoelectric generator (ATEG), where minor changes have been performed, to the exhaust system of a ULM. The TEG being analyzed in this study was initially designed to be used in cars. We have made minor modifications, mainly on the cooling of the TEG, transitioning from water-cooled to air-cooled, to evaluate if an ATEG with these minor changes is suitable for use in ULMs. Our aim is to determine if the thermoelectric generator, coupled to the engine exhaust system, can generate sufficient energy to replace the engine's alternator. Or if, on the contrary, a more specific TEG, more specific to the mission profile, aviation, would be required. This replacement would lead to a reduction in the aircraft weight, potentially increasing its flight autonomy and range. The incorporation of TEGs into the engine design, leads to the possible mitigation of the weight and energy penalties associated with traditional alternators. The exhaust system, a rich source of thermal energy, becomes a valuable reservoir for TEGs to operate, thereby reducing reliance on conventional power sources and optimizing energy utilization. The crux of our innovation lies in the unique capability of TEGs to convert waste heat into useable electrical power.

2. Research description

2.1. Engine data

Piston engines used in aircraft must exhibit a high power-to-weight ratio and low brake-specific fuel consumption. The object of study is the engine manufactured by Rotax, serving as a prime example of gasoline piston engines commonly found in ultralight aircraft. This four-cylinder boxer piston carburetor engine delivers a maximum power of 73.5 kW, making it widely utilized in the aviation industry. The cylinder arrangement enhances stability and lowers the center of gravity, resulting in a reduced total weight of the engine, as specified by the manufacturer at 59 kg [22]. The R912 shown in Fig. 1, employs air cooling for the cylinders and liquid coolant for the cylinder heads in its cooling system. This model is chosen for its favorable power to weight ratio. The key specifications of the engine are outlined in Table 1.

Fig. 1. R912 engine [22].

Table 1
Engine specifications [22].

Parameter	Description
Manufacturer	BRP-Rotax GmbH & Co KG,
Model	Rotax 912 ULS
Cylinders	4
Engine power	73.5 kW (5800 rpm)
Engine torque	128 N m
Engine type	4 strokes
Fuel consumption	15 L/h at 5000 rpm (maximum cruise speed)
Bore	84 mm
Stroke	61 mm
Cooling system	Cylinder heads: water cooled Cylinders: air cooled

2.2. Simulation software

This study utilized GT-Suite software for numerical simulations and result validation. The software's versatility allows detailed investigations into components, including vehicle emissions, engine and vehicle data (pressure, flow rate, and speed) [27]. One-dimensional modeling proved to be reliable thought this research [28]. Allowing for rapid design iterations and parameter adjustments to meet the specific requirements and objectives of the simulation process [29,30]. The engine model built with GT-suite shown in Fig. 2, depicts the schematization of the engine divided into blocks. The first block comprises the ducts which guide and distribute the external air up to the carburetors passing through the throttle. The following cluster emulates the distribution of the air/fuel mixture onto the intake valves. Cylinders and crankshaft blocks reproduce the combustion and the transformation into mechanical energy. The refrigeration process as well as all the heat and fluid dynamics processes also take, please in the aforementioned block. Lastly the exhaust system collects and guides onto the environment all the products of combustion.

Fig. 3 shows the different GT-suite elements that have been used to simulate the operation of each of the twelve thermoelectric modules of the model. Radiation and convection heat transfer from the exhaust gases to the central copper heatsink, and conduction are also considered. Afterwards, the thermal contact resistance between heatsink (hot side) and the thermoelectric module is contemplated. In TEMs heat flow is transformed into electric current, for this reason, the electric alt connectors are implemented. Consequently thermal resistance between

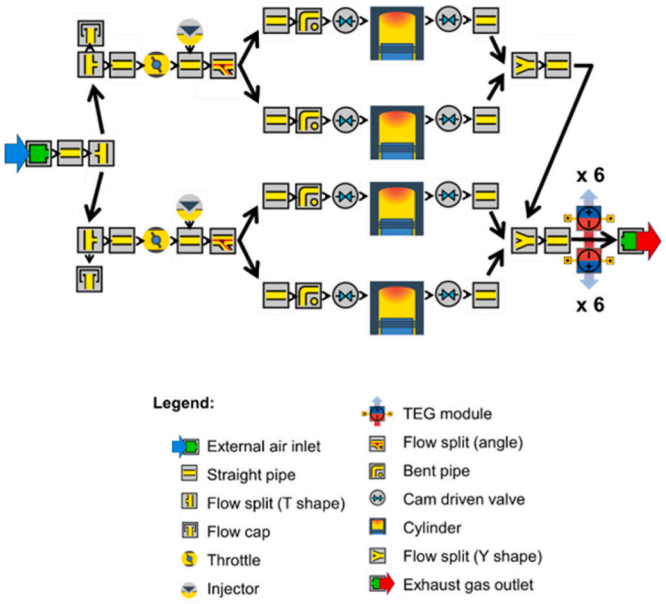

Fig. 2. Engine model in GT-Power.

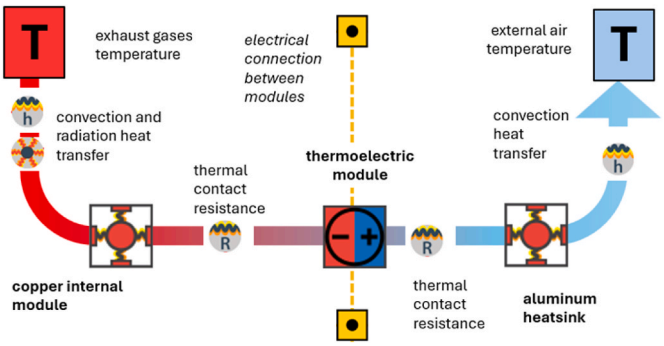

Fig. 3. TEG sub-model diagram.

TEM and heatsink (cold side) is also included. Finally, convection heat dissipation from the aluminum fin heatsink to the outside air is modeled.

2.3. Model description

The model incorporates the intake manifold, which is optional in the standard engine. The notable input measurements and values that are not provided by the manufacturer's manual were obtained from the actual engine. The geometrical data was taken from a R912, shown in Fig. 4.

The R912 is a carbureted engine. The GT-SUITE module lacks a specific tool or template for modeling a carburetor, other available tools were utilized to capture its behavior and performance. In this case, a throttle body was employed to simulate carburetor fluid dynamics, where the dimensions of the throttle body mirror those of the actual carburetors. To simulate fuel dosage, each throttle body incorporated a fuel injector, allowing for the adjustment of the Air-Fuel Ratio (AFR) as needed for each load situation. The model uses indolene as fuel, with its principal characteristics outlined in Table 2.

The discharge coefficients of the valves, in function of L/D (relationship lift-diameter of cylinder head valves) collected in Table 3, were determined through tests conducted in the flow bench at the Laboratory of Thermal Engines (University of Girona). These coefficients were extrapolated from engines with similarly arranged cylinder heads. Ideally, improvements could be made if testing could be directly performed on Rotax engine cylinder heads. The diameters for the intake and exhaust valves are 38 mm and 32 mm, respectively, as specified in the manufacturer's manual, with each cylinder having two valves. The flow bench can be seen in Fig. 5 and parameters in Table 4.

The lift and valve timing for the inlet and outlet valves are illustrated in Fig. 6, based on the data provided for the R912 engine [31]. The modeling of friction mean effective pressure (FMEP) has also been included to assess mechanical resistances.

The Chen-Flynn method as shown in eq. (1), has been chosen following the recommendations in the GT-ISE manual [32]. This method

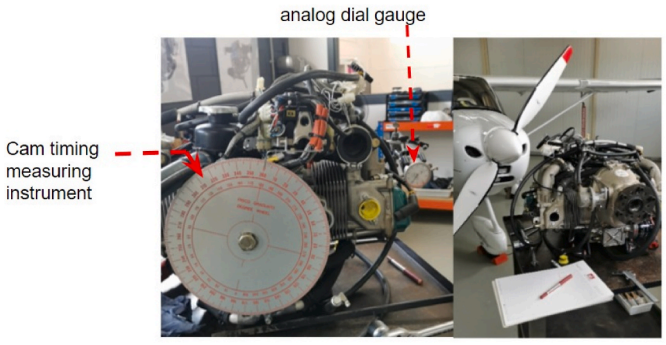

Fig. 4. Data collection from engine.

Table 2
Indolene specifications.

Parameter	Value	Units
Fuel density (at 25 °C)	750	kg/m^3
Heat of vaporization (at 25 °C)	350	kJ/kg
Lower heating value	43.95	MJ/kg

Table 3
Non dimensional valve discharge coefficients.

L/D values	Forward flow	Reverse flow
0.00	0.00	0.00
0.05	0.20	0.16
0.10	0.34	0.27
0.15	0.44	0.37
0.20	0.54	0.47
0.25	0.60	0.51
0.30	0.65	0.54
0.35	0.70	0.57

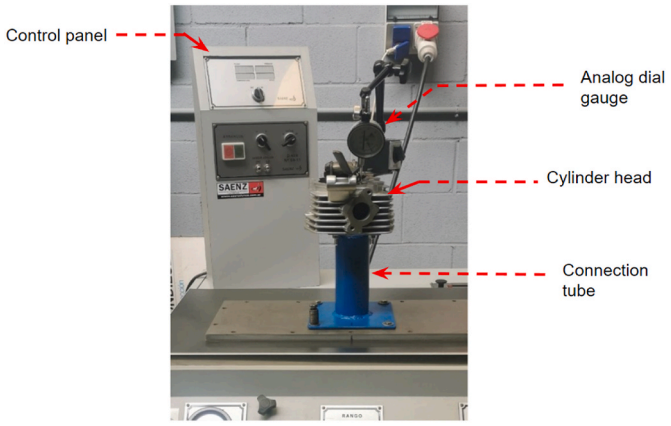

Fig. 5. Flow bench test used to obtain flow coefficient valve values.

Table 4
Flow bench characteristics.

Parameter	Description
Brand	SAENZ
Model	D-600
Maximum Flow (Exhaust/Suction mode)	$283.14{\cdot}10^{-3}$ m^3/s
Maximum Pressure (Exhaust/Suction mode)	7000 Pa
Selectable Pressure/Depression Range	250–7000 Pa
Minimum Flow (Exhaust/Suction mode)	$2.35{\cdot}10^{-3}$ m^3/s
Flow Precision	$\pm 4.71{\cdot}10^{-5}$ m^3/s
Pressure Precision	±250 Pa

employs different coefficients to consider the effects of peak and maximum cylinder pressure as well as the mean piston speed.

$$FMEP = C_{FEMP} + (F_{P.C.P} * P_{P.C.}) + (F_{M.P.S} * S_{M.P}) + (F_{S.M.P2} * S^2_{M.P.}) \quad \text{(eq. 1)}$$

where:

FMEP: friction mean effective pressure (bar)
C_{FEMP}: constant part of FMEP (bar)
$F_{P.C.P}$: peak cylinder pressure factor (0.014)
$P_{P.C.}$: maximum cylinder pressure (bar)
$F_{M.P.S}$: mean piston speed factor (0.005 bar/(m/s))
$S_{M.P}$: mean piston speed (m/s)
$F_{S.M.P2}$: mean piston speed squared factor (0.001 bar/(m/s)^2)

To model the cylinder heat transfer specifications, accurate definitions of cylinder temperatures and combustion models are essential.

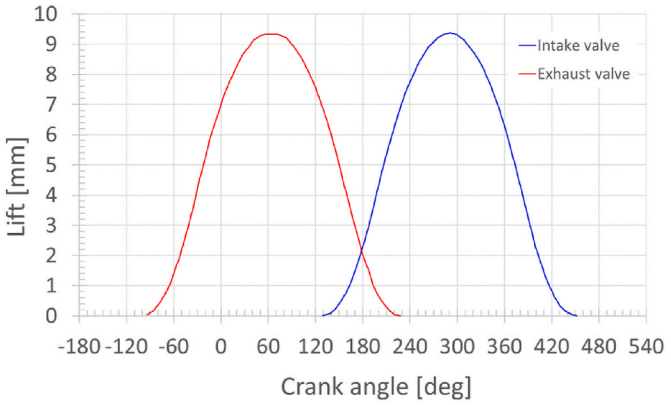

Fig. 6. Engine intake and exhaust valve lift diagram.

Different heat transfer behaviors have been considered for air-cooled cylinders and water-cooled cylinder heads, within the values recommended in the software manual. This required several iterations until values within reasonable bounds were identified to define the type of heat transfer in the cylinders and cylinder heads. For this purpose, the Woschni GT-model was selected. This model is widely used as a standard model in various industrial applications [32,33], particularly when the swirl effect is not present. As the type of cooling in the room where the engine test bench is located and the exposure of the exhaust to the ambient room air is unknown, establishing global heat transfer coefficients for the pipes and muffler of the exhaust system becomes challenging. In the process of determining heat transfer coefficients for the various segments of the exhaust system, a systematic approach involving multiple iterations was employed. The Design of Experiments (DOE) function within GT-Suite facilitated this investigation.

Simulations were conducted at three key points along the exhaust system, denoted as points 1, 3, and 5 in Fig. 13. For each simulation, two fixed parameters, gas temperature and wall temperature, were established based on actual operating conditions of the engine in the aircraft. The heat transfer coefficient, a variable parameter, was iteratively adjusted until satisfactory values were achieved. The iterations involved refining the coefficients to closely match the observed temperature distribution obtained from thermocouples. The final adopted values for heat transfer coefficients were determined based on the convergence of the simulated temperature maps with the experimental data obtained from the temperature sensors at each identified point. These values were found to be 140 W/m2·K for the first segment after the cylinder head, 25 W/m2·K for the muffler, and 65 W/m2·K for the final part of the exhaust. The sensors specifications and arrangements are shown in Table 12.

The combustion model employed, in the absence of experimental records of pressures inside the combustion chamber, involves a two-zone model with Wiebe combustion modeling. The Wiebe combustion model is utilized to calculate the energy release rate per crank angle. This model is particularly suitable for describing the combustion of premixed fuel and air in a spark-ignition engine cycle. The Wiebe function is defined as follows [32]:

$$Combustion(\theta) = (CE)\left[1 - e^{-(WC)(\theta - SOC)^{(E+1)}}\right] \quad \text{(eq. 2)}$$

where:

θ: crank angle (degree)
E :Wiebe exponent (values set between 2 and 3)
CE :fraction of fuel burned (also known as "combustion efficiency" set to 1)
WC :Wiebe constant defined by eq.3
SOC :starting angle of combustion (degrees) defined by eq. (4).

$$WC = \left[\frac{D}{BEC^{1/(E+1)} - BSC^{1/(E+1)}}\right]^{-(E+1)} \quad \text{(eq. 3)}$$

$$SOC = AA\left[\frac{(D)(BMC)^{1/(E+1)}}{BEC^{1/(E+1)} - BSC^{1/(E+1)}}\right]^{-(E+1)} \quad \text{(eq. 4)}$$

$$BMC = -ln(1 - BM) \quad \text{(eq. 5)}$$

$$BSC = -ln(1 - BS) \quad \text{(eq. 6)}$$

$$BEC = -ln(1 - BE) \quad \text{(eq. 7)}$$

where:

D: combustion length (25–35° crank angle).
AA: anchor angle (5° to 12°).
BM: percentage of fuel burned at a certain anchor angle (50 %).
BS: percentage of fuel burned at the beginning of combustion (10 %).
BE: percentage of fuel burned at the end of combustion (90 %).
BMC: burned midpoint constant.
BSC: burned start constant.
BEC: burned end constant.

For the combustion parameters, optimization was performed until the maximum peak pressure was achieved between 12° and 13° CA after PMS. The effect of exhaust gas recirculation has not been considered in any of the cases.

2.4. TEG design specification

The final design for the generator is based on a design of a TEG used in the automotive sector originally designed by us [34] where we have replaced the liquid refrigeration circuit with air cooling. Shown in Fig. 7, and its specifications are in Table 5.

The heat absorber, or hot-side heat exchanger, of this TEG consists of a copper plate with dimensions of 210 × 140 × 15 mm (length × width × height). It features six cylindrical holes, each with a diameter of 12 mm. The heat absorber incorporates a total of 12 commercial thermoelectric modules six on each face of the heat absorber.

In our simulation, the cool side of the TEG has been adapted using a system of air-cooling fins, manufactured by the Miba group company. These fins are in contact with ambient air, and their temperature is dependent on flight altitudes, with initial conditions set at 0 m and 15 °C. The aluminum cooling fins are strategically distributed along the two cold sides of the TEG, there are a total of 84 fins with a dimension of 200 × 25 × 0,5 mm (length × width × thickness) and a spacing of 3 mm between fins. The total surface area exposed to ambient air is 840 × 10^3 mm^2. While TEG modules are typically characterized by relatively large volumes and sizes in the context of aircraft applications where space and weight constraints are critical the bulkiness of traditional TEGs is not ideal. By creating a more streamlined and compact TEG module, the goal is to reduce overall volume and weight, addressing the constraints imposed by the limited space available in aircraft applications. The introduction of a novel design, incorporating thinner yet efficient materials, aims to optimize the TEG's form factor for aircraft installations while preserving its effectiveness in power generation [34].

Table 5
TEG element description.

Number	Description
1	Heat absorber gas exchanger copper plate with six cylindrical holes (TEMs hot side)
2	12 TEMs (TELBP1-12656-0.45) Thermonamic Electronics Corp. Nanchang, China
3	Finned aluminum heatsink cooled by air (TEMs cold side)
4	Inlet/outlet exhaust pipe connectors

3. Model validation

In the first validation stage, the simulation model underwent testing using data provided by the manufacturer present in the operator's manual [31], including engine torque, power, and fuel flow consumption values. These values, obtained at full throttle and partial loads along the propeller curve, covered a wide range of engine speeds shown in Table 6.

The second step of the validation process involved testing using experimental data obtained at partial loads close to the propeller curve

Table 6
Manufacturer partial load throttle angle values along propeller curve.

Throttle angle (°)	Engine speed (rpm)
90	5800
62	5500
37	5000
24	4500
18.5	4000
16.5	3500
15	3000
10	2500

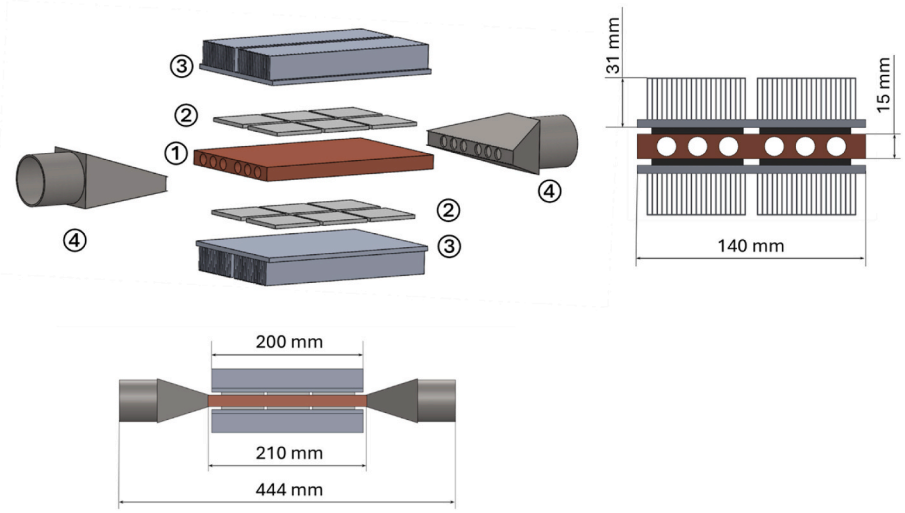

Fig. 7. TEG design diagram.

shown in Table 7.

Fig. 12 and Table 11 depict the setup of the sensors utilized for conducting experiments for experimental data collection. Fig. 8 illustrates the location of the temperature measuring points in the original engine exhaust system. Sensors no. 1 and 2 were placed in the section of individual exhaust pipes from the cylinders, while sensor no. 3 was positioned in the exhaust pipe behind the silencer [26,35,36]. Previous analysis focused on six strategic points in the exhaust system to determine exhaust gas and exhaust pipe temperature distribution at selected points in relation to engine speed and loads [37]. It was determined that the engine exhaust manifold could successfully serve as a heat source for a thermoelectric generator. It was suggested that, due to high temperature values rising well over the temperature limit for TEMs, direct installation on manifold walls might not be possible. Consideration that we have acknowledged when building the final TEG design.

Experimental load points selected for validating the model at partial loads were those closest to the propeller curve. This curve illustrates the horsepower required to move the propeller with a fixed angle of attack at various engine speeds. The parameters considered include power, fuel consumption, brake specific fuel consumption (BSFC), and temperatures. For temperature analysis, we closely examined points 1 and 3 as depicted in Fig. 8. The significance of point number 1 is due to the fact that its location is closest to the cylinder and can yield values of the initial gas temperature after combustion. Point 3 is crucial as it is at the end, where we can see how the gas could have cooled after passing through the exhaust system and it is also where we positioned the TEG. Additional testing points were introduced along the exhaust structure to gather supplementary temperature data, enabling us to assess temperature distribution and variations along the system. In the final phase, to assess the model's capability to simulate engine behavior at altitudes different from sea level, we compared the results with the manufacturer data. The tested altitudes ranged from 4300 to 5800 m above sea level.

3.1. Model validation based on manufacturer data

As illustrated in Fig. 9, the simulation effectively captures the general trend of increasing power with engine speed, as expected based on the manufacturer's specifications. This confirms the model's robustness in predicting the behavior of engine power output. Due to the lack of comprehensive input data for all engine speeds, the model was primarily constructed using information available for nominal engine speeds and conditions closely related to these speeds. The data is illustrated in Table 8 (see Fig. 10).

The data shared by the manufacturer provided values of power and torque along the propeller curve at different engine speeds. The propeller curve, Fig. 11, is necessary to determine the required horsepower to turn the installed propeller at various engine speeds Table 9.

3.2. Model validation based on experimental data

We validate the engine model with the experimental data available to us, utilizing the values presented in Table 10. These values are crucial, as they are not provided by the manufacturer. These values provide more in-depth information regarding the parameters we aim to analyze,

Table 7
Experimental partial loads throttle angle values.

Throttle angle (°)	Engine speed (rpm)
66	5765
60	5519
52	5012
45	4567
29	4063
26	3445
21	2981
14	2529

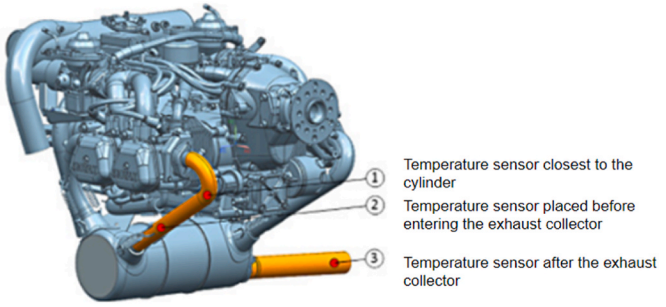

Fig. 8. Arrangement of the sensors in the engine exhaust system without turbocharger.

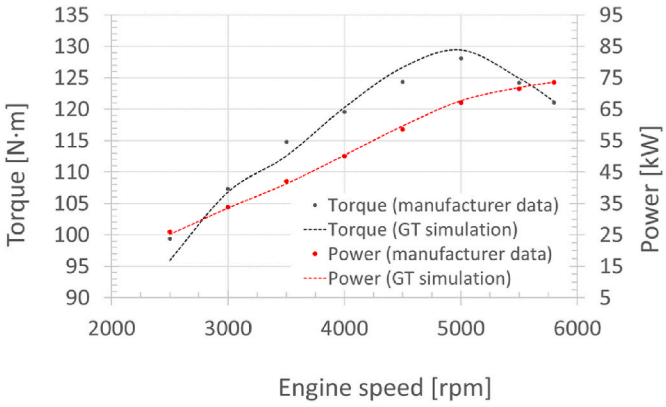

Fig. 9. Comparison at full throttle data provided by the manufacturer and simulations for engine power and torque.

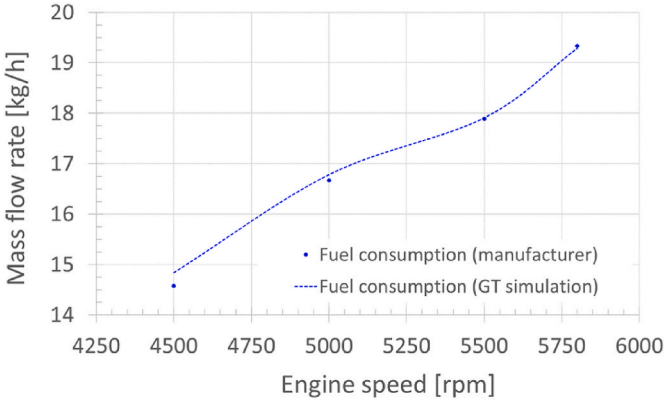

Fig. 10. Comparison of fuel consumption at full throttle data provided by the manufacturer and simulations.

Table 8
Operator's manual data used in model validation at full throttle.

Engine speed [rpm]	Torque [N·m]	Power [kW]	Fuel mass flow [kg/h]
2500	99.4	26.0	No data
3000	107.3	33.8	No data
3500	114.8	42.1	No data
4000	119.6	50.1	No data
4500	124.3	58.6	14.6
5000	128.1	67.1	16.7
5500	124.2	71.5	17.9
5800	121.0	73.5	19.3

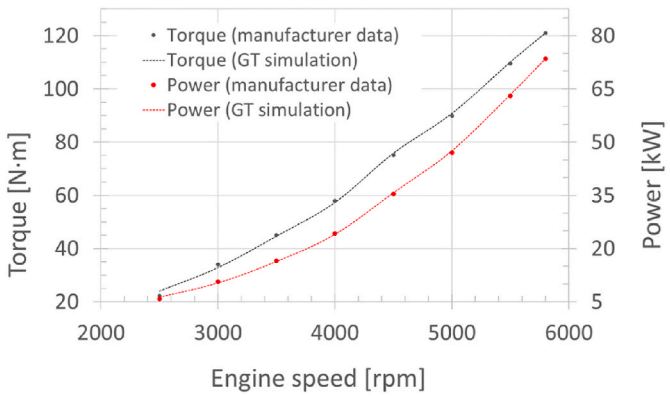

Fig. 11. Comparison along propeller curve of data provided by the manufacturer and simulations for engine power and torque.

shown in Figs. 14 and 15.

The data was obtained thought extensive testing carried in the Centre for Innovation and Advanced Technologies of the Lublin University of Technology. The engine set up can be seen in Fig. 12. Test stand specifications are in Table 11.

The placement of the sensors is crucial in order to efficiently analyze the engine performance. The engine is equipped with an array of varying sensors ranging from, engine's speed monitors, to exhaust temperature monitors. These are located at different positions through the exhaust system. The temperature measuring points along the exhaust system are shown in Fig. 14 and sensor specifications in Table 12.

To validate the temperatures obtained by the model, since the manufacturer does not provide such data, we utilized the data obtained experimentally, comparing the same points to affirm the model's accuracy [37]. Our analysis indicated that the data generated by our model closely aligns with that of the experimental study, Fig. 16, confirming the accuracy of our model for further testing and integration of thermoelectric generators.

3.3. Model validation based on flight altitude

The manufacturer provides performance data at various flight altitudes and engine speeds. This is of importance as engine performance will vary due to the decreased air density found at higher altitudes. The engine model is tested at two different engine speeds 4300 rpm and 5800 rpm, both at full throttle. The flight altitudes tested range from 0 m

Table 9
Propeller curve values used for validation.

Engine speed [rpm]	Power [kW]	Torque [N·m]
2500	5.8	16.6
3000	10.7	18.8
3500	16.5	21.0
4000	24.3	24.0
4500	35.4	25.6
5000	47.1	27.1
5500	63.1	28.0
5800	73.5	27.5

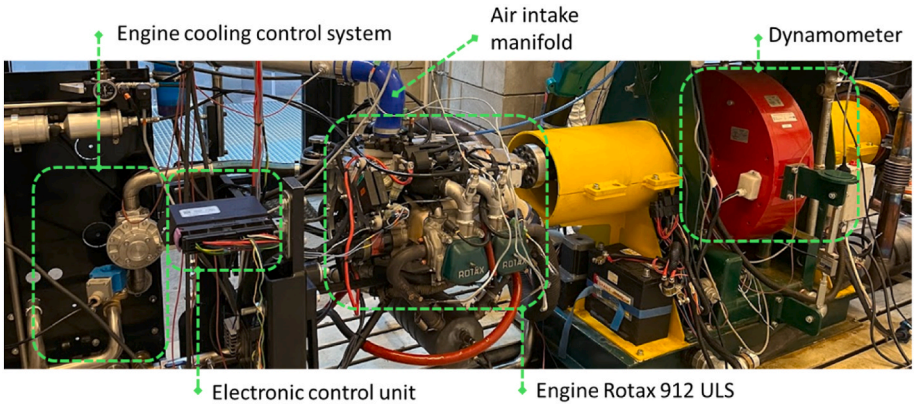

Fig. 12. Rotax engine installed on test stand.

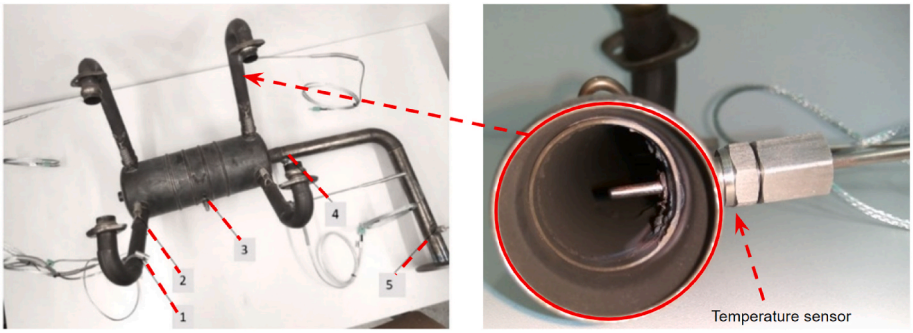

1. Temperature sensor closes to the cylinder
2. Temperature sensor closest to exhaust muffler
3. Temperature sensor within exhaust muffler
4. Temperature sensor immediately after exhaust muffler
5. Temperature sensor at the end of the exhaust tail pipe

Fig. 13. Exhaust system of R912 engine and temperature sensor installed.

Table 10
Experimental values collected from test bench conducted at Lublin University.

Engine speed [rpm]	Power [kW]	Torque [Nm]	Fuel mass flow [kg/h]	Lambda –	AFR [kg/kg]	T1 [°C]	T5 [°C]
2529	10.6	40.1	3.35	0.90	13.230	563.2	390.6
2981	17.0	54.5	5.04	0.90	13.230	624.9	478.9
3445	25.8	71.6	8.03	0.85	12.495	653.4	556.4
4063	34.0	79.9	10.26	0.85	12.495	683.8	613.5
4567	46.9	98.1	13.57	0.85	12.495	699.9	671.0
5012	53.5	101.9	15.30	0.85	12.495	723.0	695.4
5519	64.0	110.8	17.89	0.85	12.495	745.9	717.9
5765	69.9	115.8	19.33	0.85	12.495	760.3	731.7

Table 11
Test stand equipment with make and model.

Parameter	Description
Test bench	Automex 200
Operation conditions	Steady-state and load conditions
Brake system	Electric motor brake connected to the test object through a cardan shaft
Electro-mechanical brake	Elektromex Centrum EMX - 200/6000 braking power up to 200 kW at the rotational speed up to 6000 rpm
Dynamometer control system	Automex SP. z o.o. ATMX 2000
Gravimetric fuel conditioning and meter system	Automex SP. z o.o. ATMX 240
Cooling system	Oil: heat exchangers - Engine: cooling water - Brake external cooling
Measurement system	Tektronix TCP305 current probes - TCP A300 converters - Data acquisition cards - National Instruments NI CompactDAQ-9184 module
Data processing software	LabVIEW
Experimental modification	Carburetor replaced with an electronic fuel injection system, maintaining the original carburetor's diameter and length

Table 12
Experimental setup and measurement instruments specifications of the exhaust system temperature analysis.

Parameter	Specifications
Exhaust system temperature measurements	Standard ROTAX engine exhaust system
Measurement distances	30 mm, 180 mm, 400 mm, 600 mm, 1000 mm
Thermocouples	Type K (NiCr–NiAl) by Czaki Thermo – Product
Exhaust gas temperature sensors	TP-204K-1b-150-1
Temperature sensors for exhaust system elements	TP-203K-1b-150-1
Measurement devices	NI 9213 measuring devices by National Instruments
Integration system	Four-socket, Ethernet, and USB transmission system
Data acquisition (DAQ) module	Processes signals from the measuring card and digitally transmits to the computer

up to 7500 m, corresponding to the limits provided by the manufacturer Fig. 17.

4. The effect on the engine with TEG incorporated

We aim to analyze the engine's performance and behaviour when the TEG is attached to the R912. By introducing the TEG, which is typically not part of the standard exhaust system, we aim to assess its impact on the engine's performance. We evaluate the results obtained from various simulations where the TEG is coupled to the engine, against the values previously collected from the manufacturer and experimental data. Fig. 18 illustrates the engine power as function of rotational speed. Ranging from 2500 to 5800 rpm at partial loads under atmospheric sea

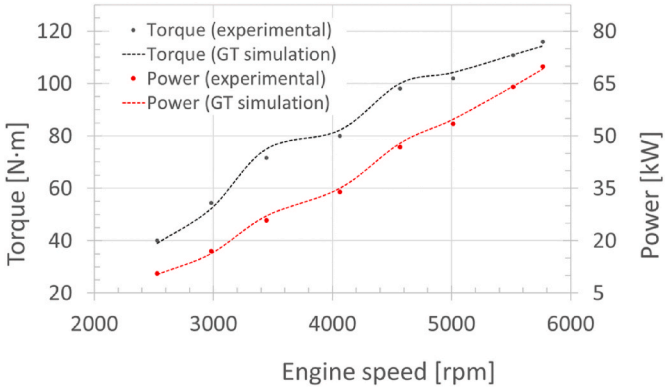

Fig. 14. Comparison of experimental power and torque versus simulated values.

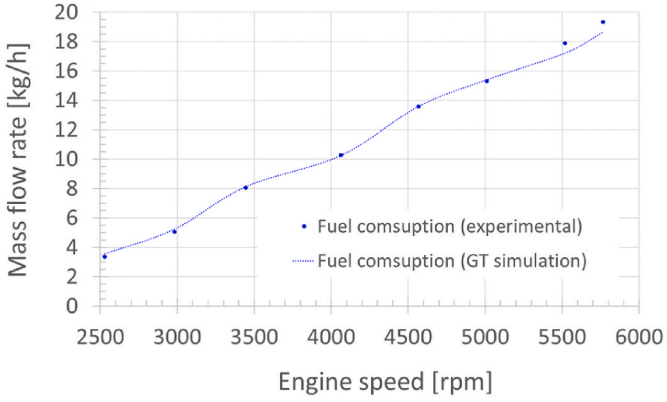

Fig. 15. Comparison of experimental data vs simulated mass fuel flow consumption.

level conditions. The simulation results, particularly under maximum load conditions, reveal a torque curve that slightly deviates from the values provided by the manufacturer. The expected tendency is that the engine with TEG shall produce higher power outputs than the manufacturer. When comparing the power output to the experimental data at the same loads the engine with TEG falls under the expected values. This observation is crucial as it indicates that the attachment of the TEG to the model leads to a notable decline in engine performance, as evidenced by the graphs.

The output power difference between the engine coupled with the TEG and the engines without, can be attributed to the back pressure generated by the design of the pipes and connecting surfaces. The heat absorber in our TEG is a copper block with six cylindrical holes of 12 mm inner diameter. This geometric configuration introduces more back pressure compared to heat absorbers based on fins [38]. However, heat exchangers with cylindrical holes have some advantages over heat

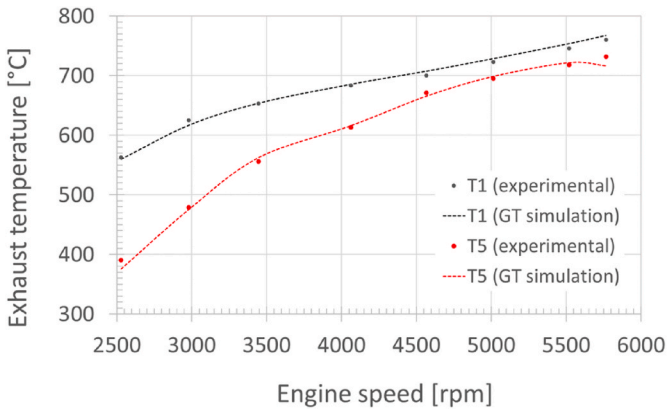

Fig. 16. Experimental temperatures recorded at points 1 and 5 of the exhaust system and the simulated values comparation.

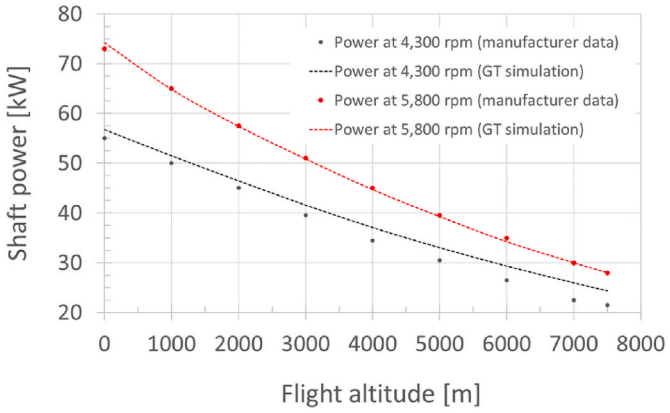

Fig. 17. Power at 4500 and 5800 rpm for different altitudes, comparison between data given by the manufacturer and simulations.

absorbers with fins. The latter have constraints related to the type of material being used, and the geometrical dimensions of the fin (minimum available fin spacing and fin thickness depending on the manufacturing techniques) [34].

In Fig. 19, we can observe a direct relationship between the volumetric flow of gases and the backpressure being generated. As the gas flow increases, the backpressure rises exponentially. This observed phenomenon is crucial in understanding the impact of backpressure on engine performance. The backpressure generated by the thermoelectric generator (TEG) adds to the overall backpressure from the muffler. This combination of backpressure helps explain why the model with the TEG is exhibiting reduced power and torque. Backpressure significantly influences the thermodynamic cycle of the engine, particularly during the exhaust phase, leading to increased head losses and the retention of residual exhaust gases inside the cylinder.

Monitoring the fuel demand, in relation to power is crucial to determine how modifications to the engine alter its performance. An increase could lead to a diminution in flight autonomy, countering the primary goal of extending flight range through the coupling of the TEG. This is illustrated in Fig. 20, where the brake specific fuel consumption (BSFC) of the model with TEG differs from the curve produced by the model without. The model without the generator demonstrates higher efficiency. The difference can be attributed to the backpressure introduced by the addition of the TEG, requiring an increase in fuel demand to produce adequate horsepower for the engine.

5. Electrical production

We obtained electric power production by the TEG at maximum and various loads and engine speeds. We compared the electric power obtained with the temperature of the gases at point 5 of the exhaust system. Fig. 21 demonstrates that higher exhaust temperatures are associated with increased electric power generation. The most significant differences between temperature and electric power occur at low engine speed. As, lower revolutions result in lower exhaust temperatures, leading to reduced electric power generation. An additional crucial factor influencing electric power production from the TEG is the exhaust mass flow of gases, which is also included in Fig. 21.

The electric power generated at full engine throttle increases with a direct correlation to temperature and mass flow. Although, when looking at high engine speeds and loads, when the mass flow of gases continues to increase the temperature decreases. On the graph, it is shown that this leads to a reduction in the electric power produced, demonstrating that the system is more sensitive to temperature than the mass flow of gases.

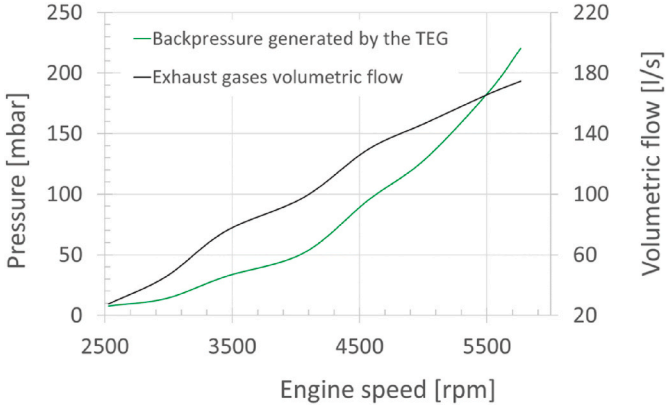

Fig. 19. Simulated TEG backpressure.

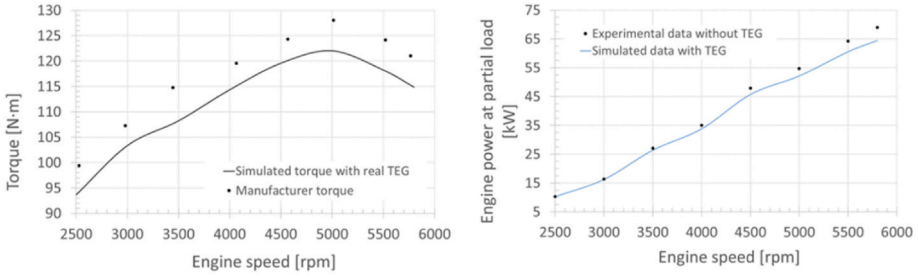

Fig. 18. Comparison of power at partial loads (b), and full load (a).

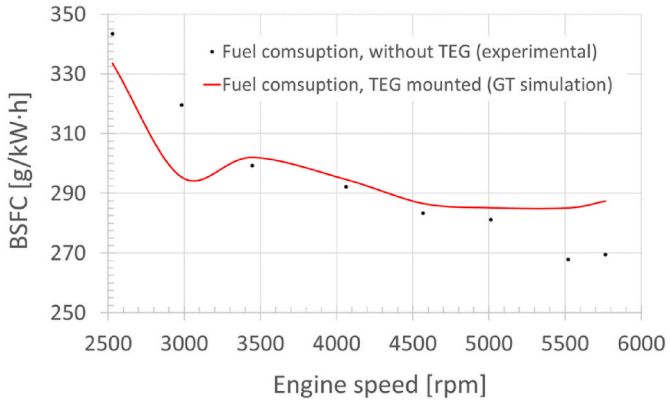

Fig. 20. Break specific fuel consumption (BSFC) with TEG mounted and without TEG at partial loads.

Based on our simulations and available data [26], the electric power produced by the TEG would be sufficient to supply energy to the fuel injection kit, which has a total power demand of 140.34 W as per Table 13. This suggests the potential to replace and eliminate the need for the alternator.

6. Results for an ideal TEG design

The primary objective of our study was to assess the capabilities of the TEG coupled to the exhaust system of an ultralight aircraft. The aim was to produce sufficient energy to power all the electric systems on the airplane. Throughout the investigation it was sought to determine the feasibility of removing alternators, thereby reducing aircraft weight, and increasing fuel autonomy. It was observed that the analyzed TEG introduced significant backpressure, resulting in a consequent reduction in power and torque compared to manufacturer and experimental data. Hence, we made the decision to transform the real TEG into an "ideal TEG," eliminating the effects of backpressure. Once this adjustment was implemented, we found that removing alternators became a viable option, as power and torque increased when the backpressure issue was resolved, leading to a more efficient engine. Our analysis included the assessment of power generated by the alternator [26], which depends solely on engine speed. Notably, we observed that the alternator produced more power than required by the aircraft's electronics, with a power demand of 140.34 W, a demand already met by the TEG. The power produced by the alternator was determined from experimental data, and these values are illustrated in Fig. 22.

To incorporate the impact of increased power resulting from the removal of the alternator into the model and simulate various load scenarios effectively, the alternator power has been converted to brake mean effective pressure, Table 14, denoted as $bmep_{alt}$ shown in eq (8).

$$bmep_{alt} = \frac{N_{alt} \bullet 2}{n \bullet V_d} \quad \text{(eq. 8)}$$

where:

$bmep_{alt}$: break mean effective pressure equivalent for alternator [bar].

N_{alt}: power consumption of alternator [W].

n: engine speed [rad/s].

V_d: total engine volume displacement [m^3].

Subsequently, the engine has been simulated with its original

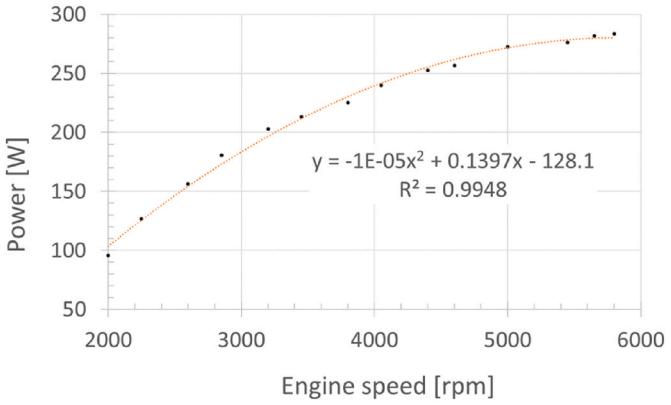

Fig. 22. Alternator electrical power produced at different engine speeds (experimental data).

Table 13
Power demand by the fuel injection system.

Element	Model	Electric power [W]
Fuel pump	Bosch 044	120.00
Lambda sensor	LSU 4.2	10.00
Fuel injector	Edelbrock 3583	9.60
Throttle position sensor	BEI Duncan 9851	0.15
Hall effect gear tooth sensor	Honeywell IGT101DC	0.12
Air temperature sensor	KTY 19-6M	0.12
Coolant temperature sensor	KTY 19-6M	0.12
Engine control unit	ROTAX ECU V01	0.10
Air pressure sensor	Honeywell PX2JG2250KA	0.07
Fuel pressure sensor	Honeywell PX2AG110BAA	0.07
Total		**140.35**

Table 14
Break mean effective pressure values for corresponding engine speed.

Engine speed [rpm]	Bmep alternator [bar]
2500	0.052
3000	0.054
3500	0.054
4000	0.053
4500	0.051
5000	0.048
5800	0.043

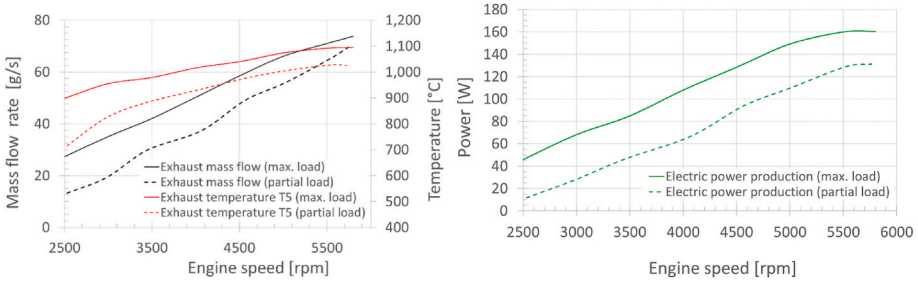

Fig. 21. Exhaust temperature and mass flow rate (left) and electric power production (right) at different loads.

configuration, without TEG, and under laboratory conditions of 15 °C and 1013 mbar ambient pressure, with an engine speed between 2500 rpm and 5800 rpm and with a throttle position between 10° and 90°. Obtaining a map of fmep values based on the Chenn-Flynn equation. As the elimination of the alternator has the effect of reducing the engine's friction losses, its $bmep_{alt}$ can be perfectly assimilated to a friction mean effective pressure $fmep_{alt}$, and this value can then be deduced in each of the corresponding rpm cells obtained from the simulation. The graph of the corrected fmep values for the engine without alternator and an ideal TEG is shown in Fig. 23.

Therefore, in models studying the engine behavior without the alternator, it is sufficient to introduce the corrected fmep values in the form of a dependent XYZ table so that the software uses only these values. The data is extrapolatable to all simulations carried out under sea level conditions, as the Chenn-Flynn equation uses coefficients that depend, among other parameters, on the combustion chamber pressure, which varies according to the flight altitude. Consequently, in the case of landing and take-off scenarios, if the flight altitude is below 4000 m, it could be assumed that the fmep varies little or not at all. Hence, once we removed the alternator, we decided to run the simulation on the new engine models without the alternators to determine the performance shown in Fig. 24 and Table 15.

It is noticeable that once the alternators are removed, the power and torque production experience an increase, improving engine performance and decreasing the specific fuel consumption. As shown in Fig. 26, the BSFC at max load decreases between 0.10 % and 0.72 % in reference to the simulated original engine configuration (without ideal TEG), indicating that the engine will be more efficient. Data in Table 16,. If we compare the results of the mass fuel flow consumption shown in Fig. 25, the fuel savings during take-off will be in the order of 0.55 %, corresponding to the engine speed where the alternator produces the maximum power.

The condition at maximum load is only utilized during take-off, limited to 5 min according to the manufacturer's specifications. Therefore, it is better to focus the study on specific fuel consumption along the load points closest to the propeller curve. These studied load points align with those obtained experimentally at partial load, as shown in Table 10.

To obtain fuel savings, the model without the alternator (with Ideal TEG) was modified using the Design Optimizer tool on GT-Suite. This involved finding the optimal throttle positions to deliver the same power and torque as the model with the alternator. As expected, once the power and torque were equated between the models, the Brake Specific Fuel Consumption (BSFC) of the model without the alternator was reduced.

We can observe, based on Fig. 26 and Table 17, that the expected fuel savings at partial loads closest to the propeller curve vary from 1.42 to 0.40 %. During the cruise phase of the airplane, where the engine speed generally ranges between 3500 and 5000 rpm, the expected fuel economy averages around 0.61 %. As the airplane initiates the landing phase,

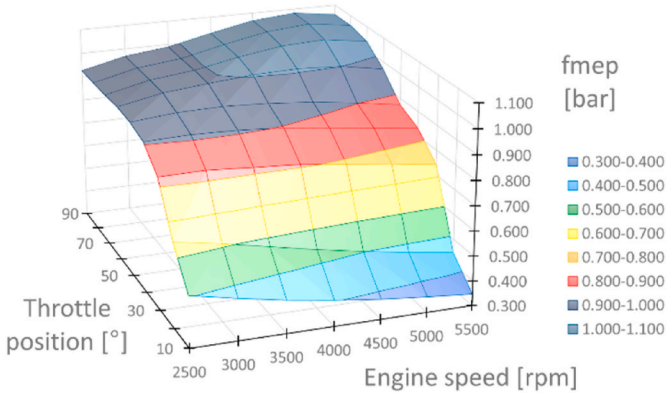

Fig. 23. Map of *fmep* corrected for the engine without alternator.

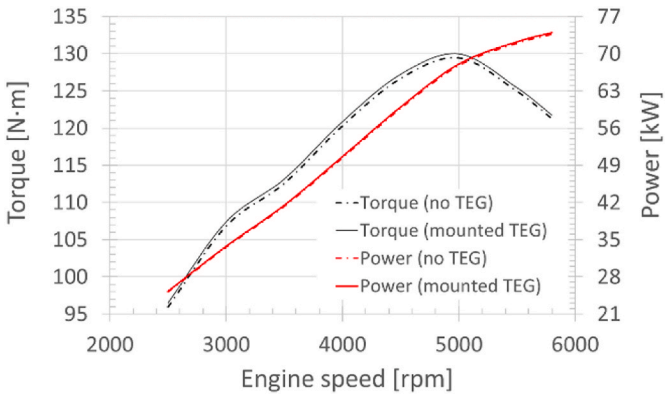

Fig. 24. Simulated engine power and torque at maximum load with, and without an ideal TEG.

Table 15
Max load performance with and without an ideal TEG.

Engine speed [rpm]	Power w/ Ideal TEG [kW]	Power w/o TEG [kW]	Torque w/ideal TEG [N·m]	Torque w/o TEG [N·m]
5800	73.9	73.7	121.7	121.3
5500	72.2	71.9	125.4	124.9
5000	68.1	67.8	129.9	129.5
4500	59.9	59.7	127.2	126.7
4000	50.6	50.4	120.9	120.3
3500	41.5	41.3	113.2	112.6
3000	33.7	33.6	107.4	106.8
2500	25.3	25.1	96.5	95.9

Table 16
Brake specific fuel consumption and mass fuel flow at max load.

Engine speed [rpm]	BFSC w/ ideal TEG [g/kWh]	BFSC w/o ideal TEG [g/kWh]	BFSC difference [%]	Mass Fuel flow w/o ideal TEG [kg/h]	Mass Fuel flow w/ ideal TEG [kg/h]
5800	261.1	261.8	0.28	19.33	19.22
5500	247.1	248.9	0.72	17.89	17.82
5000	246.1	247.6	0.60	16.67	16.64
4500	247.8	248.6	0.35	14.64	14.64
4000	250.6	251.9	0.51	No data	12.67
3500	254.1	255.4	0.52	No data	10.54
3000	258.9	260.4	0.57	No data	8.74
2500	269.0	269.3	0.11	No data	6.84

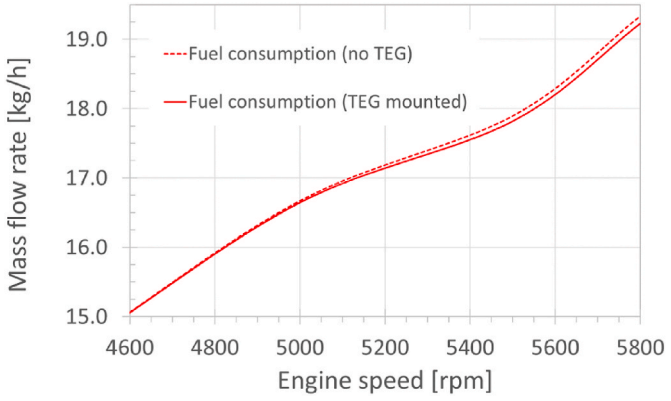

Fig. 25. Fuel consumption at maximum load, with and without an ideal TEG mounted.

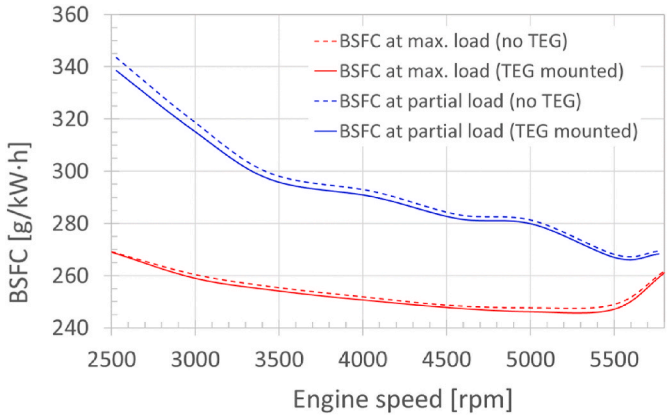

Fig. 26. BSFC compared at maximum and partial load, and the influence of an ideal TEG mounted.

Table 17
BSFC partial loads with and without an ideal TEG mounted.

Engine speed [rpm]	BSFC w/ideal TEG [g/kW-h]	BFSC w/o ideal TEG [g/kW-h]	BSFC difference (%)
5765	268.4	269.5	0.40
5519	266.7	267.9	0.43
5012	279.8	281.2	0.49
4567	281.9	283.4	0.54
4063	290.2	292.2	0.69
3445	296.9	299.3	0.77
2981	316.0	319.6	1.10
2529	338.6	343.5	1.42

the engine speed decreases and is situated close to 3000 rpm or below, leading to an expected fuel economy of about 1.10 %. Understandably, the major fuel savings during a normal flight are obtained during the cruise phase due to the significant amount of time spent in this flight phase.

We have quantified the expected fuel savings of two schools that integrate our TEG onto their aircraft fleet (see Table 18).

All airplanes are single engine except for the P2006T, which is a multi-engine aircraft. Hence if the school has four of this model, this will account for 8 engines in total.

For a normal day of operation, the usual flight time will be a 3 h flight in the morning and 3 h in the afternoon. Taxi time will be an additional 20 min in the morning and again in the afternoon. For taxi the plane will operate at 2529 RPM, and 4063 RPM during cruise.

To determine the fuel saved per kWh, we first computed the difference in BSFC (g/kWh) between the engine with the TEG and without it. We then multiplied this difference by the number of hours the engine operates under the specific flight configuration and by the engine's power output (kW) during that time. This calculation provided us with the total amount of fuel saved. The values are collected in Table 19.

We proceeded to compute the fuel savings at different RPMs for the different planes that make up the school's fleet. Values present in Table 20.

The table quantifies the fuel savings for two fleets demonstrating that significant fuel savings can be achieved over time when integrating the

Table 18
Flight school fleet.

School A	School B
P2002JF (9)	P2002JF (2)
P2006T (4)	P2006T (4)
P2008JC (5)	P2008JC (9)
	P-Mentor (2)

Table 19
Fuel saving computation.

Time spent: 40 min	0,668	hours	Time spent: 6 h	6	hours
BSFC with TEG:	338.6	g/kWh	BSFC with TEG:	290.2	g/kWh
BSFC without TEG:	343.5	g/kWh	BSFC without TEG:	292.2	g/kWh
Percentage difference:	1.42	%	Percentage difference:	0.69	%
k/Wh:	10.26 (Fig. 18 (b))	kW	k/Wh:	33.82	kW
RPM	2529		RPM	4063	
kWh difference:	4.90	g/kWh	kWh difference:	2.00	g/kWh
Fuel saved per kWh:	**23.8**	**g**	**Fuel saved per kWh:**	**607.2**	**g**

TEG into an aircraft fleet. While the observed BSFC % difference was higher at lower RPMs leading to a more noticeable fuel savings per hour, the total fuel savings over longer periods are greater at higher engine speeds despite the lower BSFC % difference. This is due to the fact that an aircraft typically spends more time operating at higher RPMs during flight resulting in cumulative savings.

Successful implementation of our TEG design into an aircraft fleet can positively impact flight operations as we are able to reduce substantially fuel usage. Displaying the benefits of successful integration of TEGs into light aviation enhancing fuel efficiency and reducing operational costs.

7. Conclusions

After analyzing the data obtained, the following conclusions can be highlighted:

- We successfully validated the simulation model using GT-Suite software, enabling us to estimate the electrical power generated by the thermoelectric generator. Detailed performance analysis of the R912 was conducted across different engine speeds, altitudes and configurations, with and without TEG. The analysis provided valuable insights into how the engine's performance is affected by the presence of the TEG.
- By replacing the traditional alternator with a TEG not specifically design for aviation, the study indicated that it could be effectively adapted for use in ultralight aircraft. By using a TEG, we were able to produce and harvest enough electrical energy to feed the fuel injection kit, thereby showcasing its potential for improving the efficiency and functionality of aircraft systems. However, while we successfully adapted an automotive TEG for aviation purposes, it is important to highlight that to maximize the ultimate potential of TEGs, a specific one designed for aviation needs to be developed. An ATEG is sufficient for initial adaptation, but it is not quite optimal. The feasibility of using existing automotive technologies in new contexts is promising and can potentially reduce development costs and time for creating aviation-specific TEGs, but further optimization and specialized design are essential for achieving the best performance and integration.
- It has been proven that not only is it important to maximize the electrical power generated by the TEG, but an optimal design of the heat sink is also essential. The internal geometry of the heatsink, in contact with the combustion gases, generates pressure losses, which must be minimized to ensure the correct operation of the combustion engine.
- The integration of TEGs in light aircraft has been shown to be beneficial in terms of fuel savings, with more substantial long-term benefits realized at higher engine speeds despite lower percentage differences in BSFC. The successful adaptation of TEG technology

Table 20
Fuel saving quantification.

School: A	2529 rpm (40 min)		4063 rpm (6 h)		School: B	2529 rpm (40 min)		4063 rpm (6 h)	
P2002JF (9)	214.2	g	5464.8	g	P2002JF (2)	47.6	g	1214.4	g
P2006T (4)	380,8	g	9715.2	g	P2006T (4)	380.8	g	9715.2	g
P2008JC (5)	119	g	3036	g	P2008JC (9)	214.2	g	5464.8	g
					P-Mentor (2)	47.6	g	1214.4	g
In one day of operation	**One month**		**One year**		**In one day of operation**	**One month**		**One year**	
13.4 kg	**401 kg**		**4817 kg**		**12 kg**	**383 kg**		**4598 kg**	

highlights its potential to enhance the efficiency of aviation systems, making a strong case for further research and development in this area.

The study opens avenues for future research, such as exploring lightweight materials and advanced manufacturing techniques for TEG components to further reduce weight and improve integration into aircraft systems. Suggestions for further improvement include constructing a propeller model coupled with the engine model for detailed flight phase analysis, modifying the TEG structure to minimize backpressure, and designing a TEG specific to light aviation to determine its viability and maximize its potential.

CRediT authorship contribution statement

Iho López Tobi: Writing – review & editing, Writing – original draft, Visualization, Validation, Resources, Project administration, Methodology, Investigation, Formal analysis, Data curation, Conceptualization. **Martí Comamala:** Writing – review & editing, Writing – original draft, Visualization, Validation, Resources, Project administration, Methodology, Formal analysis, Data curation, Conceptualization. **Lino Montoro:** Writing – review & editing, Supervision, Project administration, Methodology. **Josep Ramon González:** Project administration. **Jacek Czarnigowski:** Supervision, Resources, Investigation, Data curation. **Arantzazu Gómez:** Writing – review & editing, Conceptualization.

Declaration of competing interest

The authors declare that they have no known competing financial interests or personal relationships that could have appeared to influence the work reported in this paper.

Acknowledgements

The authors would like to acknowledge the owners of the Airsport Viladamat company for giving us free access to their hangars and allowing us to take data from the engines.

Data availability

Data will be made available on request.

References

[1] Airbus S. A.S. Flying by numbers: global market forecast for 2015-2034. France; 2015. https://espas.secure.europarl.europa.eu/orbis/document/flying-numbers-global-market-forecast-2015-2034.
[2] García-Contreras R, Soriano JA, J A, Gómez A, Fernández-Yáñez P. Sustainable alternatives for aviation fuels. Elsevier; 2022. p. 177–99. https://doi.org/10.1016/B978-0-323-85715-4.00009-4 [Chapter 7] - Biojet fuels and emissions.
[3] Rosser JC, Vignesh V, Terwilliger BA, Parker BC. Surgical and medical applications of drones: a comprehensive review. J Soc Laparoendosc Surg 2018;22(3). 10.4293%2FJSLS.2018.00018.
[4] SolmanG G. (Air force tech. Sgt., 163rd attack wing). Air force drones help California firefighters combat wildfires. U.S. Department of Defence; 2017. https://www.defense.gov/News/News-Stories/Article/Article/1348274/air-force-drones-help-california-firefighters-combat-wildfires/.
[5] Li Z, Liu Y, Hayward R, Zhang J, Cai J. Knowledge-based power line detection for UAV surveillance and inspection systems. 23rd international conference image and vision computing New Zealand. 2008. https://doi.org/10.1109/IVCNZ.2008.4762118.
[6] The Royal Veterinary College. European project ID: 812904: AIRSCAN, a customised low-cost ultralight aircraft for survey, filming and animal tracking in wild environments. https://doi.org/10.3030/812904; 2020.
[7] Nicolosi F, De Marco A, Sabetta V, Della Vecchia P. Roll performance assessment of a light aircraft: flight simulations and flight tests. Aero Sci Technol 2018;76:471–83. https://doi.org/10.1016/j.ast.2018.01.041.
[8] Neves AF, Lawson NJ, Bennett CJ, Khanal B, Hoff RI. Unsteady aerodynamics analysis and modelling of a Slingsby Firefly aircraft: detached-Eddy Simulation model and flight test validation. Aero Sci Technol 2020;106:106179. https://doi.org/10.1016/j.ast.2020.106179.
[9] Czarnigowski J, Skiba K, Dubieński K. Investigations of the temperature distribution in the exhaust system of an aircraft. Combustion Engines 2019;177–2:11–8. https://doi.org/10.19206/CE-2019-203.
[10] Nicolosi F, De Marco A, Della Vecchia P. Stability, flying qualities and longitudinal parameter estimation of a twin-engine CS-23 certified light aircraft. Aero Sci Technol 2013;24–1:226–40. https://doi.org/10.1016/j.ast.2011.11.011.
[11] Strategic Research and Innovation Agenda (SRIA). Advisory Council for aviation research and innovation in Europe, vol. 1; 2017. https://www.dlr.de/dlr/Portaldata/1/Resources/documents/2017/acare-strategic-research-innovation-volume-1-v2.7-interactive.pdf.
[12] Massaguer E, Massaguer A, Pujol T, Gonzalez JR, Montoro L. Modelling and analysis of longitudinal thermoelectric energy harvesters considering series-parallel interconnection effect. Energy 2017;129:59–69. https://doi.org/10.1016/j.energy.2017.04.061.
[13] García-Contreras R, Agudelo A, Gómez A, Fernández-Yáñez P, Armas O, Ramos Á. Á. Thermoelectric energy recovery in a light-duty diesel vehicle under real-world driving conditions at different altitudes with diesel, biodiesel and GTL fuels. Energies 2019;12:1105. https://doi.org/10.3390/en12061105.
[14] Gou JJ, Yan ZW, Hu JX, Gao G, Gong CL. The heat dissipation, transport and reuse management for hypersonic vehicles based on regenerative cooling and thermoelectric conversion. Aero Sci Technol 2021;108:106373. https://doi.org/10.1016/j.ast.2020.106373.
[15] Gao G, Li D, Gou JJ, Gong CL, Li SM. A study of interfacial electrical contact resistances of thermoelectric generators for hypersonic vehicles by experimental measurements and two-scale numerical simulations. Aero Sci Technol 2022;131:107966. https://doi.org/10.1016/j.ast.2022.107966.
[16] Matlock J, Warwick S, Sharikov P, Richards J, Suleman A. Evaluation of energy efficient propulsion technologies for unmanned aerial vehicles. Trans Can Soc Mech Eng 2019;43:481. https://doi.org/10.1139/tcsme-2018-0231. 48.
[17] Fasano G, Accardo D, Tirri AE, Moccia A, De Lellis E. Radar/electro-optical data fusion for non-cooperative UAS sense and avoid. Aero Sci Technol 2015;46:436–50. https://doi.org/10.1016/j.ast.2015.08.010.
[18] Cheng Kunlin, Jiang Qin, Jiang Yuguang, Lv Chuanwen, Zhang Silong, Wen Bao. Performance assessment of multi-stage thermoelectric generators on hypersonic vehicles at a large temperature difference. Appl Therm Eng 2017;66:12–9. https://doi.org/10.1016/j.applthermaleng.2017.11.057.
[19] Cheng Kunlin, Jiang Qin, Sun Hongchuang, Dang Chaolei, Zhang Silong, Liu Xiaoyong, Wen Bao. Performance assessment of an integrated power generation and refrigeration system on hypersonic vehicles. Aero Sci Technol 2017;89:192–203. https://doi.org/10.1016/j.ast.2019.04.006.
[20] Wang Yilin, Cheng Kunlin, Dang Chaolei, Wang Cong, Qin Jiang. Hongyan Huang Performance and experimental investigation for a novel heat storage-based thermoelectric harvester for hypersonic vehicles. Energy 2023;263. https://doi.org/10.1016/j.energy.2022.125885. Part D.
[21] Ziolkowski Pawel, Zabrocki Knud. Eckhard müller TEG design for waste heat recovery at an aviation jet engine nozzle. Appl Sci 2018;2637. https://doi.org/10.3390/app8122637.
[22] Rotax powertrains. Datasheet aircraft engine Rotax 912. https://www.flyrotax.com/products/912-uls-s; 2023.
[23] Otkur M. Altitude performance and fuel consumption modelling of aircraft piston engine Rotax 912 S/ULS. Journal of Advanced Research in Applied Sciences and Engineering Technology 23-1 2021. https://doi.org/10.37934/araset.23.1.1825.
[24] Kreyer JO, Müller M, Esch T. A map-based model for the determination of fuel consumption for internal combustion engines as a function of flight altitude. Deutscher Luft- und Raumfahrtkongress; 2019. https://doi.org/10.25967/490162.
[25] Mansouri H, Ommi F. Performance prediction of aircraft gasoline turbocharged engine at high-altitudes. Appl Therm Eng 2019;156:587–96. https://doi.org/10.1016/j.applthermaleng.2019.04.116.
[26] Skiba K, Czarnigowski J. Electric energy balance of the ROTAX 912 with fuel injection. Journal of KONES Powertrain and Transport 2017;24–1. https://doi.org/10.5604/01.3001.0010.2834.

[27] Gamma Technologies. GT-SUITE. Integrated multi-physics system simulation. Gamma technologies. 2023. https://www.gtisoft.com/gt-suite/.
[28] Carlucci AP, Ficarella A, Laforgia D, Renna A. Supercharging system behaviour for high altitude operation of an aircraft 2-stroke diesel engine. Energy Convers Manag 2015;101:470–80. https://doi.org/10.1016/j.enconman.2015.06.009.
[29] Lebedevas S, Dailydka S, Jastremskas V, Rapalis P. The influence of locomotive diesel engine transient operating modes on energy usage. Transport Res Part D 2015;34:219–29. https://doi.org/10.1016/j.trd.2014.10.011.
[30] Li H, Shi L, Deng K. Development of turbocharging system for diesel engines of power generation application at different altitudes. J Energy Inst 2016;89:755–65. https://doi.org/10.1016/j.joei.2015.04.001.
[31] BRP-Powertrain. Operator's manual for ROTAX engine type 912 series. OM-912, Ver 4.0; 2012. https://rotax.my.salesforce-sites.com/DocumentsSearch/sfc/servlet.shepherd/version/download/0685c00000IhJYnAAN?asPdf=false.
[32] Gamma technologies. Engine performance application manual. 2018.
[33] Heywood JB. Internal combustion engine fundamentals. second ed. McGraw-Hill Education; 2018.
[34] Comamala M, Ruiz I, Massaguer A, Massaguer E, Pujol T. Effects of design parameters on fuel economy and output power in automotive thermoelectric generator. Energies 2018;11:3274. https://doi.org/10.3390/en11123274.
[35] Czarnigowski J, Skiba K, Rękas D, Ścisłowski K, Jakliński P. Bench tests for exhaust gas temperature distribution in an aircraft piston engine with and without a turbocharger. Adv Sci Technol 2021;15–3:155–66. https://doi.org/10.12913/22998624/139688.
[36] Syta A, Czarnigowski J, Jaklinski P. Detection of cylinder misfire in an aircraft engine using linear and non-linear signal analysis. Measurement 2021;174:108982. https://doi.org/10.1016/j.measurement.2021.108982.
[37] Comamala M, Pujol T, Ruiz I, Massaguer E, Massaguer A. Power and fuel economy of a radial automotive thermoelectric generator: experimental and numerical studies. Energies 2018;11:2720. https://doi.org/10.3390/en11102720.
[38] Li X, Wang Z. Exergy analysis of integrated TEG and regenerative cooling system for power generation from the scramjet cooling heat. Aero Sci Technol 2017;66:12–9. https://doi.org/10.1016/j.ast.2017.02.021.